


Effects of WEC Geometry on the Performance of a WEC Array-VLFS Integrated System

Zhiyang Zhang  ^{1,2}

Linpei Dai  ¹

Ziheng Wang  ³

Haitao Wu  ^{4*}

¹ School of Ocean Engineering, Jiangsu Ocean University, Lianyungang, China

² College of Marine Engineering, Jiangsu Ocean University, Lianyungang, China

³ Makarov College of Marine Engineering, Jiangsu Ocean University, Lianyungang, China

⁴ Department of Naval Architecture, Ocean and Marine Engineering, University of Strathclyde, Glasgow, United Kingdom

* Corresponding author: haitao.wu@strath.ac.uk (Haitao Wu)

ABSTRACT

This study focuses on analysing the effects of wave energy converter (WEC) geometry on the performance of an integrated system comprising a WEC array and a very large floating structure (VLFS). A numerical model of the integrated system is established based on multi-body potential theory, the discrete-module-beam (DMB) method, and the Lagrange multiplier technique. After validating the accuracy of the simulation approach, the present study examines the energy capture efficiency and hydroelastic response of the integrated system with various WEC geometry parameters, including length, width, draft, and shape. Owing to the complexity of the physical model of the integrated system, it is difficult to determine the optimal Power Take-Off (PTO) damping coefficient analytically. Therefore, a numerical search method is employed to obtain the PTO damping coefficients corresponding to different WEC geometry parameters. After a series of numerical simulations, the results reveal that, compared to the other three geometry parameters, the power output of the integrated system is more sensitive to the WEC length. Moreover, the incorporation of the WEC array leads to a significant reduction in the hydroelastic response of the VLFS. In addition, the draft and shape of the WEC exhibit limited influence on the structural response of the VLFS. All in all, the analytical methodology and framework presented in this paper can offer some insights for the design of similar integrated systems.

Keywords: WEC geometry, WEC array-VLFS integrated system, energy capture performance, hydroelastic response

INTRODUCTION

The extensive consumption of traditional energy sources and increasingly severe environmental issues has led to growing worldwide emphasis on the development of renewable energy [1,2]. Among these, the ocean is one of the significant sources of renewable energy [3,4]. It should be noted that, among various forms of renewable marine energy, wave energy has attracted considerable attention due to its high energy density and all-day operational capability [5,6]. Based on energy conversion mechanisms, wave energy converters (WECs) are mainly

categorised into oscillating bodies, oscillating water columns, and overtopping devices [7]. Of these three types, oscillating-body devices have become one of the most favoured options, owing to their simple geometric structure and suitability for array configurations [8]. Although scholars have extensively researched oscillating-body WECs, their commercial development has not yet been fully realised, primarily due to high energy costs [9]. Therefore, integrating oscillating-body WEC arrays with other marine structures may present a viable solution, as it can save space, share facilities, reduce costs, supply energy, and provide structural protection.

When incident waves interact with the WECs, a portion of the wave energy is absorbed, while the remaining unabsorbed energy transmits through the WECs. Consequently, the transmitted wave height downstream of the WEC is significantly reduced. Breakwaters are designed to attenuate waves from the open sea and provide sheltered areas for marine aquaculture and port engineering. Therefore, WECs and breakwaters share a common principle in wave absorption, which has drawn increasing attention to hybrid systems integrating oscillating-body WECs with floating breakwaters. Moreover, integrating the WECs into a breakwater can further enhance wave energy conversion through relative motions between the floating bodies. Zhao et al. [10] applied an analytical potential model to conduct a hydrodynamic analysis of a WEC-breakwater hybrid system, demonstrating that the incorporation of WECs can absorb wave energy without compromising the wave attenuation performance of the breakwater. Ning et al. [11] established a two-dimensional mathematical model of a dual-floater system serving as both breakwater and WEC. Their simulations revealed that, compared to a single floater, the two-floater system significantly broadens the effective frequency band for energy capture. Zhang et al. [12] developed a frequency-domain potential model that accounts for viscous effects in a system consisting of a WEC array and a floating breakwater. Their results indicated that a WEC array positioned close to the breakwater can capture more energy and substantially reduce the horizontal forces on the breakwater. Zhou et al. [13] conducted experimental studies to determine the optimal gap width and WEC dimensions in an integrated WEC-breakwater system, with particular emphasis on evaluating the effects of narrow-gap resonance.

Very large floating structures (VLFS) have emerged as an efficient solution for marine space utilisation, owing to their low environmental impact, independence from specific seabed conditions, flexible construction, and cost-effectiveness. In recent years, such structures have been progressively applied in various fields, including floating airports, oil storage facilities, artificial floating islands, and floating piers [14]. Due to their high length-to-depth ratio, VLFSs undergo significant elastic deformation under wave action, implying that their safety and serviceability are directly governed by their hydroelastic response. Building on the advantages of integrating WECs with breakwaters, Tay [15] employed a frequency-domain finite element-boundary hybrid method to investigate an articulated plate-VLFS hybrid system, elucidating the dual role of the articulated plate as both WEC and breakwater. Nguyen et al. [16] extended this numerical approach to optimise the dimensions and layout of an array of articulated-plate WECs installed at the weather-side of a VLFS. Their study demonstrated that energy capture performance can be significantly improved by adjusting the number of WECs and the PTO damping coefficients. Cheng et al. [17] developed a numerical model for an integrated system of a heaving-type WEC array and a VLFS, based on fully nonlinear potential theory and Mindlin thick-plate theory. They further examined the effects of nonlinear interactions and wave resonance in the WEC-VLFS gap on the hydrodynamic performance of the system. Zhao et al. [18] proposed a hybrid concept involving a flexible floating platform integrated with a WEC array. Their

frequency-domain simulations revealed that neglecting platform flexibility leads to an overestimation of the energy capture efficiency of the WEC array.

Although some studies have evaluated the hydrodynamic performance of integrated WEC-VLFS systems, the influence of WEC geometry on such integrated systems has not yet been thoroughly investigated. For instance, while Cheng et al. [17] conducted a parametric study on WEC geometry, the wave energy capture in their configuration did not rely on the relative motion between the WEC array and the VLFS. Moreover, in the studies by Tay [14] and Nguyen et al. [15], the impact of WEC dimensions on system performance was primarily limited to variations in WEC length. Therefore, the motivation or novelty of this study lies in systematically examining the effects of WEC shape and other dimensional parameters—under the operational mechanism that utilises relative motion for wave energy absorption—on the performance of a WEC array-VLFS integrated system, including both the energy capture efficiency and the hydroelastic response. The analytical methodology and framework presented in this work are expected to provide new insights for the design of WEC-VLFS integrated systems, with the potential to enhance both marine space utilisation and the economic viability of wave energy development.

THEORETICAL BACKGROUND

Fig. 1 illustrates a schematic diagram of an integrated system comprising a WEC array and a VLFS. The WEC array consists of three identical oscillating bodies connected to the VLFS via Power Take-Off (PTO) units. It should be noted that, in this study, each PTO unit was simplified as a hinge joint with an equivalent linear damping coefficient. To predict the motion response of the integrated system, a numerical model was established based on the three-dimensional potential theory, employing the DMB method and Lagrange multiplier technique. The core concept of the DMB method involves discretising the VLFS into multiple rigid sub-modules, each with its mass concentrated at the centre of gravity, which are then interconnected by equivalent beam elements following Euler-Bernoulli beam theory [19]. The Lagrange multiplier technique is applied to impose kinematic constraints at the connection points, connecting each WEC to the first sub-module of the VLFS through a constraint matrix and internal force vectors [20]. The modelling procedure for the integrated system is summarised as described below.

First, based on multi-body hydrodynamics, the added mass, radiation damping, and wave excitation force matrices for the $N+3$ floating bodies (N sub-modules of VLFS and three WECs) are computed. Simultaneously, the mass and hydrostatic stiffness matrices of the integrated system are constructed. Then, the structural stiffness matrix of the entire VLFS is derived according to Euler-Bernoulli beam element theory. Subsequently, the constraint matrices for the PTO units are formulated using the Lagrange multiplier technique and, finally, all matrices are assembled to form a coupled frequency-domain model of the integrated system. A flowchart summarising the numerical modelling process is provided in Fig. 2. It should be noted that

the numerical simulations are carried out using an in-house code developed in MATLAB, which is capable of solving coupled multi-body hydrodynamics and structural dynamics.

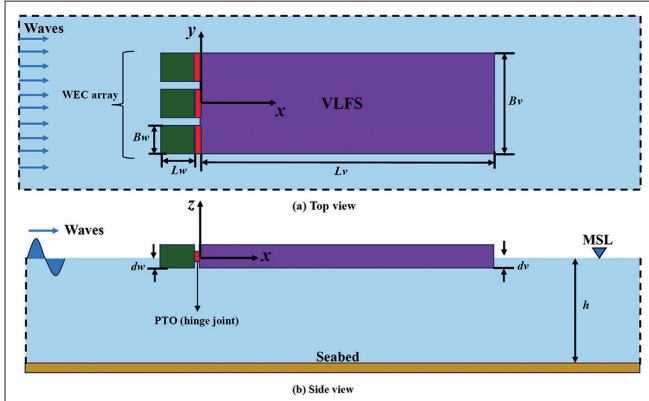


Fig. 1. Schematic diagram of the WEC array-VLFS integrated system

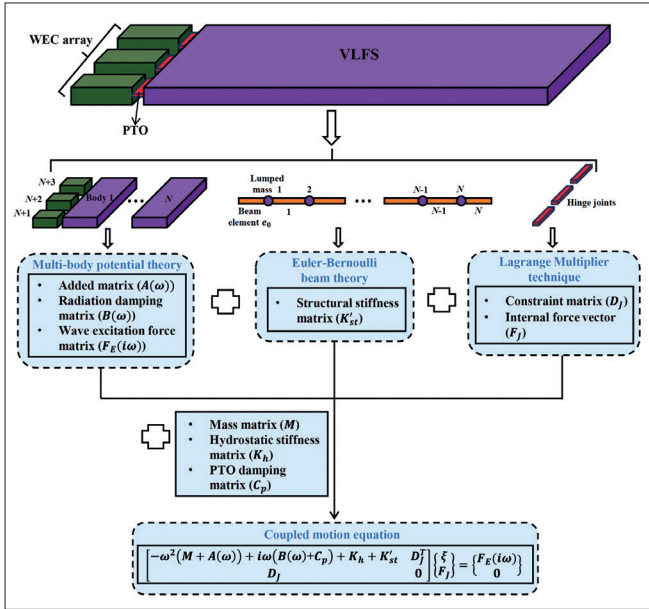


Fig. 2. Flow diagram of the numerical simulation

MULTI-BODY HYDRODYNAMICS

Within the framework of three-dimensional potential flow theory, the fluid velocity potential satisfies the Laplace equation.

$$\nabla^2 \Phi = 0 \quad (1)$$

The fluid velocity potential is composed of the incident potential Φ_I , the diffraction potential Φ_D , and the radiation potentials Φ_R from all bodies. Specifically, the radiation potential $\Phi_R^{(m)}$ of the m -th body can be expressed as:

$$\Phi_R^{(m)} = i\omega \sum_{j=1}^6 \xi_j^{(m)} \Phi_{Rj}^{(m)} \quad (2)$$

where $\xi_j^{(m)}$ denotes the complex motion amplitude of the m -th body in the j -th degree of freedom (DOF) and $\Phi_{Rj}^{(m)}$ represents the corresponding radiation potential induced by its motion.

Under finite water depth conditions, Φ_I can be expressed as:

$$\Phi_I = \frac{igA}{\omega} \frac{\cosh k(z+h)}{\cosh kh} e^{ik(x\cos\theta + y\sin\theta)} \quad (3)$$

where g is gravity acceleration; A , ω , and θ represent the wave amplitude, angular frequency, and incident direction, respectively; h denotes the water depth; and k is the wave number, which is given by the dispersion relation:

$$k = \frac{\omega^2}{g \tanh(kh)} \quad (4)$$

For the boundary value problem governing the velocity potential, the following boundary conditions must be considered:

$$-\omega^2 \Phi^x + g \frac{\partial \Phi^x}{\partial z} = 0, \quad \text{on } S_F(z=0) \quad (5)$$

$$\frac{\partial \Phi^x}{\partial z} = 0, \quad \text{on } S_B(z=-h) \quad (6)$$

$$\frac{\partial \Phi_D}{\partial \vec{n}^{(q)}} = -\frac{\partial \Phi_I}{\partial \vec{n}^{(q)}}, \quad \text{on } S_q \quad (7)$$

$$\frac{\partial \Phi_{Rj}^{(m)}}{\partial \vec{n}^{(q)}} = \begin{cases} 0, & m \neq q \\ -i\omega n_j, & m = q \end{cases}, \quad \text{on } S_q \quad (8)$$

$$\nabla \Phi^x \rightarrow 0, \quad \text{on } S_\infty \quad (9)$$

where S_F , S_B , S_q , and S_∞ denote the free surface, seabed, and wetted surface of the q -th body, and the far-field boundaries, respectively; for Φ^x , it may represent either Φ_D or $\Phi_{Rj}^{(m)}$. $\vec{n}^{(q)}$ is the normal vector on the surface of the q -th body and n_j denotes the component of the surface normal vector in the j -th DOF.

Subsequently, based on the boundary conditions outlined above, the boundary element method (BEM) is employed to numerically solve for the velocity potential [21]. The radiation potentials are then used to derive the added mass and radiation damping coefficients,

$$A_{ij}^{(q,k)} = -\frac{\rho}{\omega} \iint_{S_q} \text{Im}(\Phi_{jR}^{(k)}) n_i ds \quad (10)$$

$$B_{ij}^{(q,k)} = -\rho \iint_{S_q} \text{Re}(\Phi_{jR}^{(k)}) n_i ds \quad (11)$$

where $A_{ij}^{(q,k)}$ and $B_{ij}^{(q,k)}$ represent the added mass and radiation damping induced on the i -th DOF of the q -th body by the j -th DOF of the k -th body, respectively.

The wave excitation forces acting on the bodies, comprising the Froude-Krylov and diffraction components, are simultaneously obtained by integrating the incident and diffraction pressures over the wetted body surface,

$$F_{Ei}^{(q)} = \iint_{S_q} (P_I + P_D) n_i^{(q)} ds = -i\rho\omega \iint_{S_q} (\Phi_I + \Phi_D) n_i^{(q)} dS \quad (12)$$

Based on Eqs. (10)-(12), the added mass, radiation damping, and wave excitation force matrices of the integrated system can then be derived as:

$$A(\omega) = \begin{bmatrix} A^{(1,1)} & A^{(1,2)} & \dots & A^{(1,N+3)} \\ A^{(2,1)} & A^{(2,2)} & \dots & A^{(2,N+3)} \\ \vdots & \vdots & \ddots & \vdots \\ A^{(N+3,1)} & A^{(N+3,2)} & \dots & A^{(N+3,N+3)} \end{bmatrix}_{6(N+3) \times 6(N+3)} \quad (13)$$

$$B(\omega) = \begin{bmatrix} B^{(1,1)} & B^{(1,2)} & \dots & B^{(1,N+3)} \\ B^{(2,1)} & B^{(2,2)} & \dots & B^{(2,N+3)} \\ \vdots & \vdots & \ddots & \vdots \\ B^{(N+3,1)} & B^{(N+3,2)} & \dots & B^{(N+3,N+3)} \end{bmatrix}_{6(N+3) \times 6(N+3)} \quad (14)$$

$$F_E(i\omega) = \begin{bmatrix} F_E^{(1)} \\ F_E^{(2)} \\ \vdots \\ F_E^{(N+3)} \end{bmatrix}_{6(N+3) \times 1} \quad (15)$$

where $A^{(i,j)}$ and $B^{(i,j)}$ denote the added mass and radiation damping coefficients induced on the i -th body, due to the motion of the j -th body, and $F_E^{(i)}$ represents the wave excitation force acting on the i -th body.

STRUCTURAL DYNAMICS

As illustrated in Fig. 2, the VLFS is simplified into N concentrated mass points interconnected by beam elements. Consequently, the hydroelastic problem is transformed into the structural deformation analysis of a segmented beam subjected to external forces at its nodes [22]. This segmented beam is modelled using Euler-Bernoulli beam elements, whose axial, bending, and torsional stiffness properties are equivalently derived based on the structural parameters of the VLFS.

First, the displacements of the two nodes i and j of the beam element e_i are defined as ξ_i and ξ_j , respectively. Then, the forces generated at nodes i and j , due to structural deformation, are defined as $F_{St}^{(i)}$ and $F_{St}^{(j)}$. Finally, the relationship between the displacements and forces at the two nodes of beam element e_i can be expressed through the structural stiffness matrix as:

$$\begin{bmatrix} F_{St}^{(i)} \\ F_{St}^{(j)} \end{bmatrix} = K_e \begin{bmatrix} \xi^{(i)} \\ \xi^{(j)} \end{bmatrix} = \begin{bmatrix} K_e^{(i,i)} & K_e^{(i,j)} \\ K_e^{(j,i)} & K_e^{(j,j)} \end{bmatrix} \begin{bmatrix} \xi^{(i)} \\ \xi^{(j)} \end{bmatrix} \quad (16)$$

where K_e is the element structural stiffness matrix [23], and $K_e^{(i,i)}$, $K_e^{(i,j)}$, $K_e^{(j,i)}$ and $K_e^{(j,j)}$ are four 6×6 sub-matrices of K_e .

It should be noted that the beam elements e_0 and e_N (at both ends of the VLFS) should also be considered. For beam element e_0 , the relationship between the displacements and forces at its two nodes can similarly be described by the structural stiffness matrix as:

$$\begin{bmatrix} 0 \\ F_{St}^{(1)} \end{bmatrix} = K_0 \begin{bmatrix} \xi^{(0)} \\ \xi^{(1)} \end{bmatrix} = \begin{bmatrix} K_0^{(0,0)} & K_0^{(0,1)} \\ K_0^{(1,0)} & K_0^{(1,1)} \end{bmatrix} \begin{bmatrix} \xi^{(0)} \\ \xi^{(1)} \end{bmatrix} \quad (17)$$

After manipulating Eq. (17), the equivalent structural stiffness submatrix $\bar{K}_0^{(1,1)}$ applied to lumped mass 1 by beam element e_0 can be obtained.

$$\bar{K}_0^{(1,1)} = K_0^{(1,0)} [K_0^{(0,0)}]^{-1} K_0^{(0,1)} + K_0^{(1,1)} \quad (18)$$

Likewise, the equivalent stiffness submatrix $\bar{K}_N^{(N,N)}$ applied to lumped mass N by beam element e_N can be expressed as:

$$\bar{K}_N^{(N,N)} = -K_N^{(N+1,N)} [K_N^{(N,N)}]^{-1} K_N^{(N,N+1)} + K_N^{(N+1,N+1)} \quad (19)$$

Finally, the structural stiffness matrix of the entire VLFS can be derived as:

$$K_{St} = \begin{bmatrix} \bar{K}_0^{(1,1)} + K_1^{(1,1)} & K_1^{(1,2)} & 0 & \dots & 0 \\ K_1^{(2,1)} & K_1^{(2,2)} + K_2^{(2,2)} & K_2^{(2,3)} & \dots & 0 \\ 0 & K_2^{(3,2)} & K_2^{(3,3)} + K_3^{(3,3)} & \dots & 0 \\ \vdots & \vdots & \vdots & \ddots & \vdots \\ 0 & 0 & 0 & \dots & K_{N-1}^{(N,N)} + \bar{K}_N^{(N,N)} \end{bmatrix}_{(8 \times 6) \times (8 \times 6)} \quad (20)$$

where $K_j^{(j-1,j-1)}$, $K_j^{(j-1,j)}$, $K_j^{(j,j-1)}$ and $K_j^{(j,j)}$ are the sub-matrices of the structural stiffness matrix of the beam element e_j .

COUPLED FREQUENCY-DOMAIN MODEL

After obtaining the hydrodynamic matrices and the structural stiffness matrix, the Lagrange multiplier technique is employed to establish the coupled frequency-domain motion equation of the integrated system [24]:

$$\begin{bmatrix} -\omega^2 [M + A(\omega)] + i\omega [B(\omega) + C_p] + K_{Hy} + K'_{St} & D_J^T \\ D_J & 0 \end{bmatrix} \begin{bmatrix} \xi \\ F_J \end{bmatrix} = \begin{bmatrix} F_E(i\omega) \\ 0 \end{bmatrix} \quad (21)$$

where M and K_{Hy} represent the mass and hydrostatic stiffness matrices, respectively; C_p denotes the damping coefficient matrix of the PTO units in the integrated system; K'_{St} and D_J are the global structural stiffness matrix and the kinematic constraint matrix of the integrated system, respectively; ξ is the displacement vector of the integrated system; and F_J is the internal constraint force vector of dimension $(5 \times 3) \times 1$. ξ and F_J are the physical quantities to be solved in Eq. (21).

The mass and hydrostatic stiffness matrices (M and K_{Hy}) can be respectively formulated as:

$$M = \begin{bmatrix} m^{(1)} & & & \\ & m^{(2)} & & \\ & & \ddots & \\ & & & m^{(N+3)} \end{bmatrix}_{6(N+3) \times 6(N+3)} \quad (22)$$

$$K_{Hy} = \begin{bmatrix} C^{(1)} & & & \\ & C^{(2)} & & \\ & & \ddots & \\ & & & C^{(N+3)} \end{bmatrix}_{6(N+3) \times 6(N+3)} \quad (23)$$

where the mass and hydrostatic stiffness matrices ($m^{(n)}$ and $C^{(n)}$) of the n -th body can be found in [25].

Indeed, K_{St} in Eq. (20) only represents the structural stiffness matrix of the VLFS. Therefore, it is necessary to assemble the global structural stiffness matrix K'_{St} of the integrated system by combining K_{St} with zero matrices,

$$K'_{St} = \begin{bmatrix} K_{St} & 0 \\ 0 & 0 \end{bmatrix}_{6(N+3) \times 6(N+3)} \quad (24)$$

C_p can be expressed as:

$$C_p = \begin{bmatrix} 3\lambda_{pto} & 0 & \dots & 0 & -\lambda_{pto} & -\lambda_{pto} & -\lambda_{pto} \\ 0 & 0 & \dots & 0 & 0 & 0 & 0 \\ \vdots & \vdots & \ddots & \vdots & \vdots & \vdots & \vdots \\ 0 & 0 & \dots & 0 & 0 & 0 & 0 \\ -\lambda_{pto} & 0 & \dots & 0 & \lambda_{pto} & 0 & 0 \\ -\lambda_{pto} & 0 & \dots & 0 & 0 & \lambda_{pto} & 0 \\ -\lambda_{pto} & 0 & \dots & 0 & 0 & 0 & \lambda_{pto} \end{bmatrix}_{6(N+3) \times 6(N+3)} \quad (25)$$

where λ_{pto} is the PTO damping coefficient matrix of the individual WECs, which can be written as:

$$\lambda_{pto} = \begin{bmatrix} 0 & 0 & 0 & 0 & 0 & 0 \\ 0 & 0 & 0 & 0 & 0 & 0 \\ 0 & 0 & 0 & 0 & 0 & 0 \\ 0 & 0 & 0 & 0 & 0 & 0 \\ 0 & 0 & 0 & 0 & C_{pto} & 0 \\ 0 & 0 & 0 & 0 & 0 & 0 \end{bmatrix} \quad (26)$$

where C_{pto} is the PTO damping coefficient of the individual WECs in the 5-th DOF.

Based on the Lagrange multiplier technique, the kinematic constraint matrix D_J of the integrated system can be derived as:

$$D_J = \begin{bmatrix} D_{1,N+1} & 0 & \cdots & 0 & D_{N+1,1} & 0 & 0 \\ D_{1,N+2} & 0 & \cdots & 0 & 0 & D_{N+2,1} & 0 \\ D_{1,N+3} & 0 & \cdots & 0 & 0 & 0 & D_{N+3,1} \end{bmatrix}_{5 \times 3 \times 6(N+3)} \quad (27)$$

where

$$D_{1,N+n} = \begin{bmatrix} 1 & 0 & 0 & 0 & z_1^{(n)} & -y_1^{(n)} \\ 0 & 1 & 0 & -z_1^{(n)} & 0 & x_1^{(n)} \\ 0 & 0 & 1 & y_1^{(n)} & -x_1^{(n)} & 0 \\ 0 & 0 & 0 & 1 & 0 & 0 \\ 0 & 0 & 0 & 0 & 0 & 1 \end{bmatrix}, \quad n=1 \sim 3 \quad (28)$$

$$D_{N+n,1} = \begin{bmatrix} -1 & 0 & 0 & 0 & -z_{N+n}^{(n)} & y_{N+n}^{(n)} \\ 0 & -1 & 0 & z_{N+n}^{(n)} & 0 & -x_{N+n}^{(n)} \\ 0 & 0 & -1 & -y_{N+n}^{(n)} & x_{N+n}^{(n)} & 0 \\ 0 & 0 & 0 & -1 & 0 & 0 \\ 0 & 0 & 0 & 0 & 0 & -1 \end{bmatrix}, \quad n=1 \sim 3 \quad (29)$$

where $(x_1^{(n)}, y_1^{(n)}, z_1^{(n)})$ are the coordinates of the hinge point of the n -th PTO unit in the body-fixed coordinate system of the first sub-module of the VLFS and $(x_{N+n}^{(n)}, y_{N+n}^{(n)}, z_{N+n}^{(n)})$ are the coordinates of the hinge point of the n -th PTO unit in the body-fixed coordinate system of the n -th WEC.

After solving Eq. (21), the energy captured by each WEC can be obtained by:

$$P^{(n)} = \frac{1}{2} C_{pto} \omega^2 |\xi_5^{(N+n)} - \xi_5^{(1)}|^2, \quad n=1,2,3 \quad (30)$$

where C_{pto} is the PTO damping coefficient of the WEC; and $\xi_5^{(N+n)}$ and $\xi_5^{(1)}$ represent the displacements of the n -th WEC and the first sub-module of the VLFS, respectively.

The total energy captured by the WEC array can then be written as:

$$P_t = \sum_{n=1}^3 P^{(n)} \quad (31)$$

To characterise the energy capture performance of an individual WEC or a WEC array, the capture width ratios (CWRs) are introduced and defined as:

$$\eta^{(n)} = \frac{P^{(n)}}{B_w P_w}, \quad n=1,2,3 \quad (32)$$

$$\eta_t = \frac{P_t}{3B_w P_w} \quad (33)$$

where B_w is the equivalent width of an individual WEC and P_w denotes the incident wave power per unit width, which can be expressed as:

$$P_w = \frac{\rho g A^2 \omega}{4k} \left(1 + \frac{2kh}{\sinh 2kh} \right) \quad (34)$$

Furthermore, Fig. 3 provides a schematic illustration for determining the displacement at an arbitrary position x_{any} on beam element e . Accordingly, the relationship between the displacements and forces at node i and the arbitrary point (any) of the sub-beam element e_s can be described by the sub-stiffness matrix K_s as:

$$\begin{bmatrix} F_{St}^{(i)} \\ F_{St}^{(any)} \end{bmatrix} = K_s \begin{bmatrix} \xi^{(i)} \\ \xi^{(any)} \end{bmatrix} = \begin{bmatrix} K_s^{(i,i)} & K_s^{(i,any)} \\ K_s^{(any,i)} & K_s^{(any,any)} \end{bmatrix} \begin{bmatrix} \xi^{(i)} \\ \xi^{(any)} \end{bmatrix} \quad (35)$$

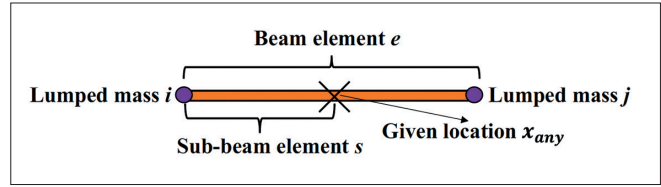


Fig. 3. Schematic diagram to calculate the displacement at any location along the VLFS

After manipulating Eq. (35), the displacement at position x_{any} can be derived as:

$$\xi^{(any)} = [K_s^{(i,any)}]^{-1} [F_{St}^{(i)} - K_s^{(i,i)} \xi^{(i)}] \quad (36)$$

where $F_{St}^{(i)}$ can be calculated using Eq. (16). Additionally, the hydroelastic response of the VLFS is one of the primary subjects of this study, of which the corresponding variable is the component of $\xi^{(any)}$ in the 3-th DOF, denoted as $\xi_3^{(any)}$.

VALIDATION OF THE NUMERICAL APPROACH

To ensure the accuracy of this study, this section presents validations of the Lagrange multiplier technique and the DMB method. For two hinged floating boxes, Fig. 4 compares the dimensionless results of the vertical displacement at the hinge and the relative rotation angle between the present simulation and the work of Newman [26]. It should be noted that Newman employed the modal expansion method to solve the motion response of the articulated model. The close agreement between the curves in Fig. 4 confirms the reliability of the Lagrange multiplier technique. Regarding the DMB method, we applied it to simulate the hydroelastic response of a typical VLFS. Fig. 5 compares the Response Amplitude Operator (RAO) obtained from this method with experimental data from Yago and Endo [27] and numerical results from Fu et al. [28]. Notably, Fu et al. employed a direct method to analyse the VLFS. The favourable agreement observed in Fig. 5 indicates that the DMB method is an accurate approach for hydroelastic analysis. Finally, detailed parameters of these two validation models can be found in the three references mentioned above.

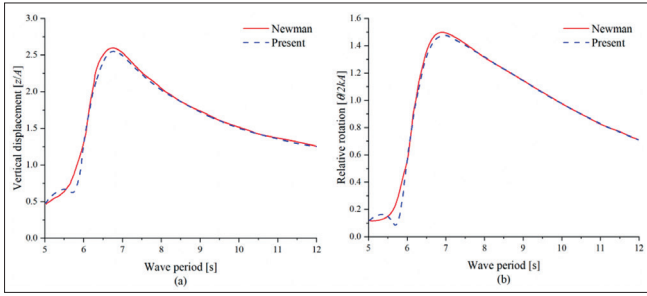


Fig. 4. Comparison of the hinge motion between Newman and the present study: (a) hinge vertical displacement; (b) hinge relative rotation

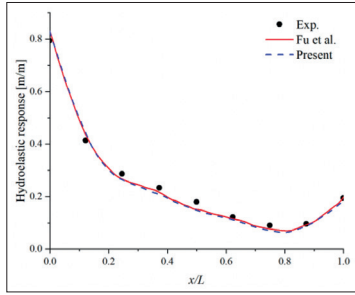


Fig. 5. Comparison of the hydroelastic response along the VLFS between Fu et al. and the present study

RESULTS AND DISCUSSION

This study investigated the influence of WEC geometry on the performance of a WEC array–VLFS integrated system, focusing on both energy capture efficiency and the hydroelastic response. The integrated system was situated in a marine environment characterised by a predominant wave period range of 5–12 s, with $T = 6$ s representing the average wave period. To maximise energy capture, the PTO damping coefficient of the WEC was generally determined based on this average period [29]. However, due to the complexity of the integrated system, an analytical solution is difficult to obtain. Therefore, a numerical search method was adopted in this study, to determine the optimal PTO damping coefficient for different WEC geometric parameters, with the detailed procedure referenced from [30]. It should be noted that, the wave amplitude and incident direction were set as $A = 1$ m and $\theta = 0^\circ$, respectively. Furthermore, Table 1 summarises the key parameters of the VLFS in the integrated system. The WEC parameters are individually introduced in the subsequent subsections. It should be noted that the centre of gravity and the radius of gyration of the VLFS and the rectangular WEC only depend on their shape. Meanwhile, the height of the WEC relative to the still water level is the same as that of the VLFS. Finally, this section analyses the system performance with respect to four aspects of the WEC geometry: length (L_w), width (B_w), draft (d_w), and shape.

In order to ensure the reliability of the numerical investigation, it was necessary to conduct a mesh convergence analysis for both the VLFS and the WEC, prior to performing the parametric analysis on the WEC geometry. According to Lu et al. [19], for a VLFS with a length of 300 m, sufficient accuracy can generally be achieved by uniformly dividing the structure into eight sub-modules along the longitudinal direction. Identical mesh

Tab. 1. Key parameters of the VLFS

Parameter	Unit	Value
Length (L_v)	m	300
Width (B_v)	m	45
Height above still water level (h_v)	m	1.5
Draft (d_v)	m	1
Mass (M_v)	kg	1.383e7
Young's modulus (E)	N/m ²	1.19e10
Poisson's ratio (ν)	–	0.13

discretisation was applied to all eight sub-modules. Therefore, in the mesh convergence analysis for the VLFS, only the weather-side module was considered. For the WEC, its geometric properties were specified as $L_w = 20$ m, $B_w = 10$ m, and $d_w = 1$ m, with a rectangular shape. This configuration served as the reference model for the subsequent parametric analysis. For both the VLFS sub-module and the WEC, three mesh discretisation strategies—coarse, medium, and fine—were adopted. Under the coarse mesh strategy, the total numbers of panels for the sub-module and the WEC were 1212 and 482, respectively. Under the medium mesh strategy, the corresponding numbers were 2496 and 704, while, under the fine mesh strategy, they increased to 4848 and 1040, respectively. After performing the hydrodynamic calculations for both the sub-module and the WEC, Fig. 6 presents their surge hydrodynamic coefficients, obtained under different mesh discretisation strategies. It can be observed that the hydrodynamic results obtained using the medium and fine mesh strategies are in close agreement, indicating that mesh convergence was achieved.

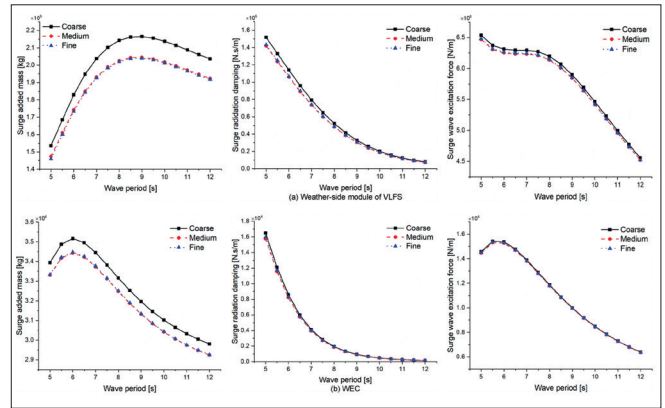


Fig. 6. Mesh convergence analysis for surge hydrodynamic coefficients: (a) Weather-side module of VLFS; (b) WEC

ANALYSIS OF DIFFERENT WEC LENGTHS

This subsection analyses the influence of WEC length (L_w) on the performance of the integrated system, with values set at 20, 25, and 30 m. The corresponding width (B_w), draft (d_w), and shape of the WECs were fixed at 10 m, 1 m, and rectangular, respectively.

Fig. 7 presents the CWR of both individual WECs and the WEC array with different values of L_w , under various wave periods. As shown in Fig. 7(a), for $L_w = 20, 25,$ and 30 m, the peak CWR of the side WEC occurs at $T = 5.5, 7.0,$ and 8.0 s, respectively. Moreover, when $L_w = 25$ m, the side WEC almost

maintains a constant power output within the period range of $T = 5.5\text{--}8.0$ s. At $T = 6.0$ s, the CWR of the side WEC varies significantly with L_w , with the highest value being observed at $L_w = 20$ m. Fig. 7(b) indicates that, for any L_w , the central WEC achieves its maximum CWR at $T = 6.0$ s. Furthermore, the energy capture efficiency of the central WEC is at its highest at $L_w = 30$ m, compared to the other two values of L_w . For $T \geq 6.0$ s, the CWR of the central WEC increases with L_w . Notably, when $L_w = 25$ m, the CWR of the central WEC is nearly zero at $T = 5.0$ s, suggesting a minimal relative angular motion at the hinge under this wave period. From Fig. 7(c), it can be observed that, for $T > 6.0$ s, the CWR of the WEC array generally increases with L_w . Similar to the central WEC, the WEC array also exhibits optimal energy capture performance at $T = 6.0$ s. However, when $L_w = 25$ m, the CWR of the array is slightly higher than that with the other two values of L_w .

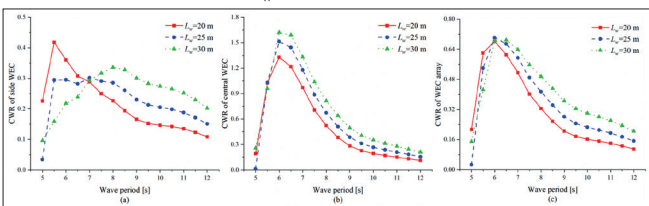


Fig. 7. (a) CWR of side WEC, (b) central WEC, and (c) WEC array with different WEC lengths under various wave periods

Fig. 8 illustrates the effects of L_w on the hydroelastic response of the VLFS. Fig. 8(a) shows that, after integrating the WEC array, the hydroelastic response of the VLFS is significantly reduced, which can be attributed to the absorption of wave energy by the WEC array. As seen in Fig. 8(b), the maximum response of the VLFS in the integrated system is lower than that of the standalone VLFS across all periods. While the maximum response of the standalone VLFS exhibits a generally increasing trend over the period range, that of the VLFS in the integrated system first decreases and then increases in the lower period range. Additionally, for $T \geq 6.0$ s, the maximum response of the VLFS shows a slightly decreasing trend with increasing L_w .

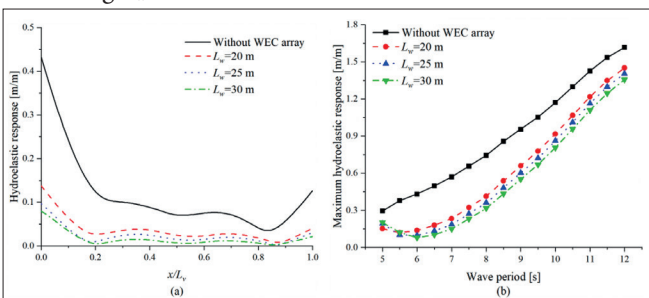


Fig. 8. (a) Hydroelastic response along the VLFS under $T=6.0$ s and (b) maximum hydroelastic response of the VLFS under various wave periods with different WEC lengths

ANALYSIS OF DIFFERENT WEC WIDTHS

This subsection examines the influence of WEC width (B_w) on the performance of the integrated system, with values set at 10, 12, and 14 m. L_w was set at 25 m, while other geometric parameters remained unchanged.

Fig. 9 presents the CWR of individual WECs and the WEC array with different B_w . As shown in Fig. 9(a), the side WEC achieves favourable energy capture performance within the period range of $T = 5.5\text{--}8.0$ s for all three B_w . At $T = 6.0$ s, the CWR of the side WEC with $B_w = 12$ m is generally higher than those at the other two B_w . In the longer period range ($T > 9$ s), the CWR of the side WEC with $B_w = 10$ m decays more slowly compared to the other B_w . It should be noted that the CWR of the side WEC starts from a very low value at $T = 5.0$ s, then increases rapidly at $T = 5.5$ s and converges toward the curves of the other two values of B_w . Fig. 9(b) indicates that, for $B_w = 10$ m and 12 m, the central WEC attains its peak CWR at $T = 6.0$ s; whereas, for $B_w = 14$ m, the maximum occurs at $T = 5.5$ s. For $T > 6.0$ s, the CWR curves for all three B_w decline monotonically with nearly identical slopes. Notably, at $T = 5.0$ s, the central WEC, with $B_w = 10$ m, captures almost no energy. From Fig. 9(c), it can be observed that the CWR of the WEC array reaches its maximum at either $T = 5.5$ s or 6.0 s for all three B_w . At $T = 6.0$ s, the energy capture performance of the array is optimal with $B_w = 12$ m, compared to the other B_w . In the long-period region ($T > 8.0$ s), the CWR of the array with $B_w = 10$ m is slightly higher than those with the other B_w , indicating better adaptability to long-period waves.

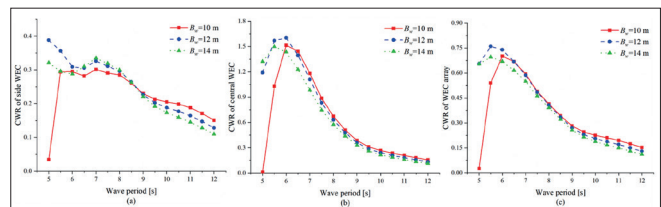


Fig. 9. CWR of (a) side WEC, (b) central WEC and (c) WEC array with different WEC widths under various wave periods

Fig. 10 illustrates the effects of B_w on the hydroelastic response of the VLFS. As shown in Fig. 10(a), the integration of the WEC array leads to a significant reduction in the longitudinal response of the VLFS. For the integrated system, increasing B_w moderately suppresses the response at the left hand side of the VLFS. However, over most of the longitudinal span of the VLFS, a larger B_w results in a slight increase in the structural response. Fig. 10(b) demonstrates that, across the entire period range, the maximum response of the VLFS in the integrated system is lower than that of the standalone VLFS. The maximum response of the standalone VLFS increases monotonically with the wave period. A similar trend is observed for the integrated system when $B_w > 10$ m. Moreover, at $T = 6.0$ s, the maximum response of the VLFS is nearly identical for $B_w = 12$ m and 14 m but slightly lower than that with $B_w = 10$ m.

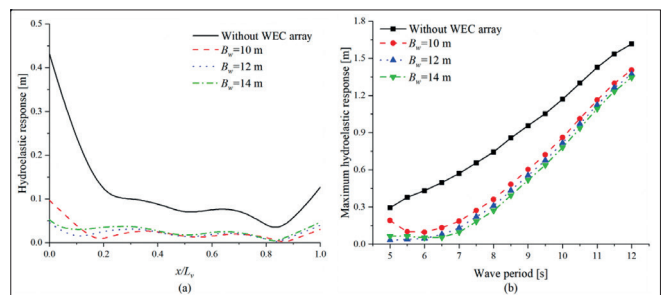


Fig. 10. (a) Hydroelastic response along the VLFS under $T=6.0$ s and (b) maximum hydroelastic response of the VLFS under various wave periods with different WEC widths

ANALYSIS OF DIFFERENT WEC DRAFTS

This subsection analyses the influence of the WEC draft (d_w) on the performance of the integrated system, with values set at 1.0, 1.5, and 2.0 m. B_w was fixed at 12 m, while other geometric parameters remained consistent with those in last section (Analysis of different WEC widths).

Fig. 11 illustrates the variation of the CWR for individual WECs and the WEC array with different drafts. As shown in Fig. 11(a), the overall trends of the CWR curves for the side WEC are similar across the three draft conditions, with peak values occurring in the lower period range ($T < 6.0$ s). Within the period range $T = 5.5\text{--}8.0$ s, the CWR of the side WEC with $d_w = 2.0$ m is higher than those with the other two d_w . For $T > 8.0$ s, the three CWR curves nearly converge. Actually, the CWR of the side WEC generally exhibits a decreasing trend with an increasing time period. Fig. 11(b) indicates that the CWR of the central WEC reaches its maximum at $T = 6.0$ s for all d_w , with the highest peak observed at $d_w = 2.0$ m. In the period range of $T = 6.0\text{--}8.0$ s, increasing d_w leads to a moderate improvement in CWR; whereas, for $T > 8.0$ s, the draft variation has negligible influence. As seen in Fig. 11(c), the CWR of the WEC array follows a similar pattern: the peak values occur around $T = 6.0$ s, and within $T = 6.0\text{--}8.0$ s, the CWR with $d_w = 2.0$ m is slightly higher than those with the other two d_w . For $T > 8.0$ s, the three CWR curves almost overlap, suggesting that the energy capture performance of the array is insensitive to draft variations in the long-period region.

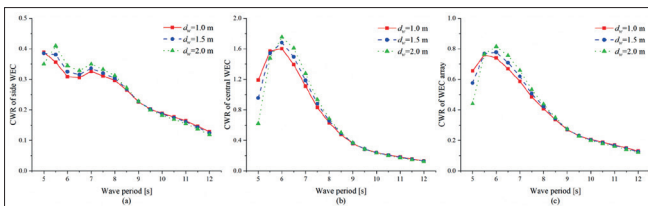


Fig. 11. CWR of (a) side WEC, (b) central WEC and (c) WEC array with different WEC drafts under various wave periods

Fig. 12 presents the hydroelastic response of the VLFS with different d_w . Fig. 12(a) shows that, at $T = 6.0$ s, the integration of the WEC array significantly reduces the longitudinal response of the VLFS, although the response curves under different d_w are very close to each other. Fig. 12(b) demonstrates that, across the entire period range, the maximum response of the VLFS in the integrated system is considerably lower than that of the standalone VLFS. Moreover, the response monotonically increases with the wave period. The differences between the three draft conditions are minimal, indicating that draft variation has limited influence on the structural response of the VLFS.

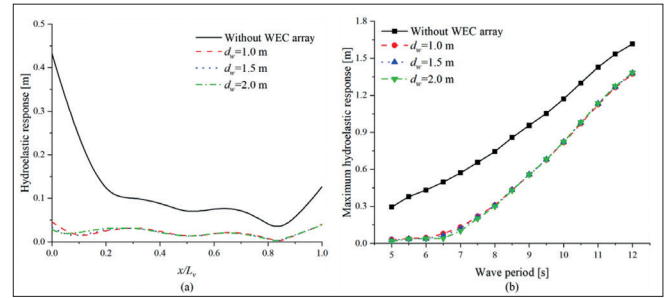


Fig. 12. (a) Hydroelastic response along the VLFS under $T=6.0$ s and (b) maximum hydroelastic response of the VLFS under various wave periods with different WEC drafts

ANALYSIS OF DIFFERENT WEC SHAPES

This subsection examines the influence of WEC shape on the performance of the integrated system. Three configurations are considered: rectangular-shape, awl-shape, and triangular-shape, as illustrated in Fig. 13. It should be noted that all three WEC types have identical mass, length, and width; their centres of gravity and radii of gyration are also identical. The draft of the rectangular WEC was set at 2.0 m, while other geometric parameters remained consistent with those in last section (Analysis of different WEC drafts).

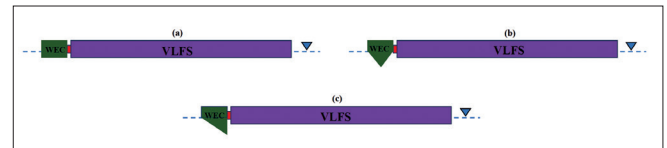


Fig. 13. Schematic diagram of the integrated system with different WEC shapes: (a) Rectangle-shape; (b) Awl-shape; (c) Triangle-shape

Fig. 14 presents the variation of the CWR for individual WECs and the WEC array with different geometries. As shown in Fig. 14(a), the CWR of the side WEC peaks at $T = 6.0$ s for all three shapes. Across the entire period range, the CWR of the triangular WEC is generally larger than those of the rectangular and awl WECs, which can be attributed to the fact that the combination of a single wave-facing slope and a deeper draft enhances effective wave excitation, whilst avoiding the dual-sided energy leakage observed in the awl-shaped design. In the longer period range ($T > 8.0$ s), all three CWR curves exhibit a declining trend. Fig. 14(b) indicates that, similar to the side WEC, the CWR of the central WEC also reaches its maximum at $T = 6.0$ s for all three geometries. For $T \geq 6.0$ s, the CWR of the triangular WEC is slightly higher than those of the other two shapes, and all three curves decline rapidly. It is worth noting that the rectangular WEC shows marginally better energy capture performance than the other two shapes at $T < 6.0$ s. This is because short waves are primarily governed by shallow-water pressure effects, such that the additional submerged volume associated with a deeper draft is not effectively excited, while the inclined faces promote wave sliding or refraction, ultimately reducing the excitation moment. As seen in Fig. 14(c), for the WEC array, the peak CWR values for all three shapes also occur at $T = 6.0$ s. Throughout the period range, the CWR of the

triangular WEC array tends to be slightly higher than those of the other two configurations. As the period increases ($T > 8.0$ s), the differences in energy capture between the three shapes gradually diminish. This suggests that the triangular shape can moderately enhance the energy capture performance of the WEC array.

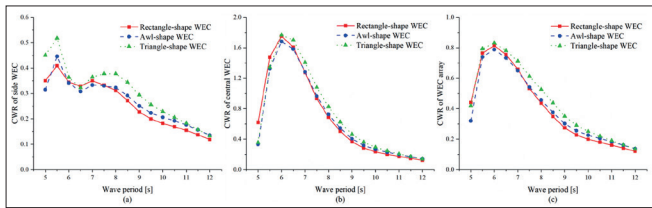


Fig. 14. CWR of (a) side WEC, (b) central WEC and (c) WEC array with different WEC shapes under various wave periods

Fig. 15 illustrates the hydroelastic response of the VLFS with different WEC geometries. Fig. 15(a) shows that, after integrating the WEC array, the longitudinal response of the VLFS is significantly reduced, while the differences between the response curves for the three shapes are minimal. Fig. 15(b) demonstrates that, across the entire period range, the maximum response of the VLFS in the integrated system is considerably lower than that of the standalone VLFS. Moreover, the maximum response gradually increases with wave period. Additionally, the response curves for the three geometries nearly overlap, indicating that the structural deformation of the VLFS is insensitive to the shape variation of the WECs.

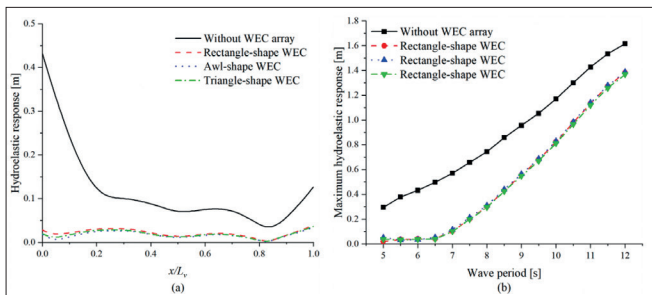


Fig. 15. (a) Hydroelastic response along the VLFS under $T=6.0$ s and (b) maximum hydroelastic response of the VLFS under various wave periods with different WEC shapes

CONCLUSIONS

Based on the potential theory, this study establishes a numerical model of a WEC array–VLFS integrated system using the DMB method and Lagrange multiplier technique, and investigates the influence of WEC geometry on its overall performance. After validating the accuracy of the numerical approach, a parametric analysis is conducted, with respect to WEC length, width, draft, and shape. According to the simulation results, the key conclusions can be summarised as follows.

In the parametric analysis of WEC geometry, the optimal energy capture performance of the WEC array consistently occurs near the average wave period. Moreover, over the average period, the energy capture efficiency of the array is more sensitive to the WEC length, compared to other geometric parameters.

After integrating the WEC array, the hydroelastic response of the VLFS is significantly reduced, compared to that of the

standalone VLFS. The maximum response of the VLFS generally exhibits an increasing trend over the entire period range. In addition, compared to the length and width, the draft and shape of the WECs have limited influence on the structural deformation of the VLFS.

Within the selected range of geometric parameters, the evaluation based on the integrated system performance at the average wave period indicates that an integrated system composed of triangular-shaped WECs with $L_w = 25$ m, $B_w = 12$ m, and $d_w = 2$ m can be regarded as a comparatively well-performing configuration.

Finally, it should be noted that this study only analyses the performance of the WEC array–VLFS integrated system in the frequency domain. Future work should address more complex challenges, such as investigating the dynamic response of the integrated system under irregular wave conditions with mooring configurations in the time domain.

ACKNOWLEDGEMENT

This paper was supported by National Natural Science Foundation of China (No. 52471284), Jiangsu Province “Qinglan Project” Outstanding Young Backbone Teacher Training Program, and MTIC-JUST Joint Innovation Center Development Fund (No. 2025MTIC-JUST003). In addition, the corresponding author would like to thank Siqi Wu for the patience, care and support over the past years.

REFERENCES

- Shi X, Liang B, Du S, Shao Z, Li S. Wave energy assessment in the China East Adjacent Seas based on a 25-year wave-current interaction numerical simulation. *Renewable Energy* 2022. <https://doi.org/10.1016/j.renene.2022.09.094>.
- Gao H, Biao L. Establishment of Motion Model for Wave Capture Buoy and Research on Hydrodynamic Performance of Floating-Type Wave Energy Converter. *Polish Maritime Research* 2015. <https://doi.org/10.1515/pomr-2015-0041>.
- Zhang Z, Guan L, Wu H, Wu L, Liu W, Cui L. Effects of the second-order hydrodynamics on the dynamic behavior of the platform among the wind-wave hybrid systems. *Journal of Engineering Research* 2024. <https://doi.org/10.1016/j.jer.2024.04.003>.
- Abbas N, Barbahan M, Kabrial Y, Kabrial A. A Novel Approach to Wave Energy Conversion Using CFD Technique. *Polish Maritime Research* 2024. <https://doi.org/10.2478/pomr-2024-0041>.
- Cui L, Wu H, Li M, Lu M, Liu W, Zhang Z. Effects of mooring failure on the dynamic behavior of the power capture platforms. *Energy* 2024. <https://doi.org/10.1016/j.energy.2024.133761>.

6. Zhang W, Zhu Y, Liu S, Wang J, Zhang W. Evaluation of Geometrical Influence on the Hydrodynamic Characteristics and Power Absorption of Vertical Axisymmetric Wave Energy Converters in Irregular Waves. *Polish Maritime Research* 2023. <https://doi.org/10.2478/pomr-2023-0029>.
7. Zhang X, Tian X, Xiao L, Li X, Lu W. Mechanism and sensitivity for broadband energy harvesting of an adaptive bi-stable point absorber wave energy converter. *Energy* 2019. <https://doi.org/10.1016/j.energy.2019.115984>.
8. Wu H, Yuan Z. Numerical investigation of the effects of short-crested irregular waves on the performance of a floating power capture platform. *Ocean Engineering* 2024. <https://doi.org/10.1016/j.oceaneng.2024.119548>.
9. He F, Huang Z, Law A-K. An experimental study of a floating breakwater with asymmetric pneumatic chambers for wave energy extraction. *Applied Energy* 2013. <https://doi.org/10.1016/j.apenergy.2013.01.013>.
10. Zhao X, Ning D, Zhang C, Liu Y, Kang H. Analytical study on an oscillating buoy wave energy converter integrated into a fixed box-type breakwater. *Mathematical Problems in Engineering* 2017. <https://doi.org/10.1155/2017/3960401>.
11. Ning D-Z, Zhao X-L, Zhao M, Hann M, Kang H-G. Analytical investigation of hydrodynamic performance of a dual pontoon WEC-type breakwater. *Applied Ocean Research* 2017. <https://doi.org/10.1016/j.apor.2017.03.012>.
12. Zhang H, Zhou B, Zang J, Vogel C, Jin P, Ning D. Optimisation of a three-dimensional hybrid system combining a floating breakwater and a wave energy converter array. *Energy Conversion and Management* 2021. <https://doi.org/10.1016/j.enconman.2021.114717>.
13. Zhou B, Lin C, Huang X, Zhang Q, Yuming Y, Zhang H, Jin P, Yang Y. Hydrodynamic performance and narrow gap resonance of WEC-floating breakwater hybrid system: An experimental study. *Ocean Engineering* 2025. <https://doi.org/10.1016/j.oceaneng.2025.121040>.
14. Gao RP, Tay ZY, Wang CM, Koh CG. Hydroelastic response of very large floating structure with a flexible line connection. *Ocean Engineering* 2011. <https://doi.org/10.1016/j.oceaneng.2011.09.021>.
15. Tay ZY. Energy extraction from an articulated plate anti-motion device of a very large floating structure under irregular waves. *Renewable Energy* 2019. <https://doi.org/10.1016/j.renene.2018.06.044>.
16. Nguyen HP, Wang CM, Flocard F, Pedroso DM. Extracting energy while reducing hydroelastic responses of VLFS using a modular raft WEC-type attachment. *Applied Ocean Research* 2019. <https://doi.org/10.1016/j.apor.2018.11.016>.
17. Cheng Y, Xi C, Dai S, Ji C, Collu M, Li M, Yuan Z, Incecik A. Wave energy extraction and hydroelastic response reduction of modular floating breakwaters as array wave energy converters integrated into a very large floating structure. *Applied Energy* 2022. <https://doi.org/10.1016/j.apenergy.2021.117953>.
18. Zhao X, Xue F, Chen L, Götteman M, Han D, Geng J, Sun S. Hydrodynamic analysis of a floating platform coupled with an array of oscillating bodies. *Ocean Engineering* 2023. <https://doi.org/10.1016/j.oceaneng.2023.115439>.
19. Lu D, Fu S, Zhang X, Guo F, Gao Y. A method to estimate the hydroelastic behaviour of VLFS based on multi-rigid-body dynamics and beam bending. *Ships and Offshore Structures* 2016. <https://doi.org/10.1080/17445302.2016.1186332>.
20. Sun L, Taylor RE, Choo YS. Responses of interconnected floating bodies. *IES Journal Part A: Civil & Structural Engineering* 2011. <https://doi.org/10.1080/19373260.2011.577933>.
21. Hess JL, Smith AMO. Calculation of non-lifting potential flow about arbitrary three-dimensional bodies. *Journal of Ship Research* 1964. <https://doi.org/10.5957/jsr.1964.8.4.22>.
22. Wu H, Liao B, Deng W, Yuan Z. Effects of hinge properties on the hydroelastic response of an interconnected very large floating structure under wave-current interactions. *Physics of Fluids* 2025. <https://doi.org/10.1063/5.0280962>.
23. Wei W, Fu S, Moan T, Lu Z, Deng S. A discrete-modules-based frequency domain hydroelasticity method for floating structures in inhomogeneous sea conditions. *Journal of Fluids and Structures* 2017. <https://doi.org/10.1016/j.jfluidstructs.2017.06.002>.
24. Zhang D-Q, Yuan Z-M, Zhao G-W, Chen Y-J, Du J-F. An experimental and numerical study of motion responses of multi-body arrays with hinge connections. *Journal of Marine Science and Engineering* 2024. <https://doi.org/10.3390/jmse12101791>.
25. Yuan Z, Incecik A, Dai S, Alexander D, Ji C, Zhang X. Hydrodynamic interactions between two ships travelling or stationary in shallow waters. *Ocean Engineering* 2015. <https://doi.org/10.1016/j.oceaneng.2015.08.058>.
26. Newman JN. Wave effects on deformable bodies. *Applied Ocean Research* 1994. [https://doi.org/10.1016/0141-1187\(94\)90013-2](https://doi.org/10.1016/0141-1187(94)90013-2).
27. Yago K, Endo H. On the hydroelastic response of box-shaped floating structure with shallow draft. *Journal of the Society of Naval Architects of Japan* 1996. <https://doi.org/10.2534/jjasnaoe1968.1998.227>.
28. Fu S, Moan T, Chen X, Cui W. Hydroelastic analysis of flexible

floating interconnected structures. *Ocean Engineering* 2007. <https://doi.org/10.1016/j.oceaneng.2007.01.003>.

29. Hu J, Zhou B, Vogel C, Liu P, Willden R, Sun K, Zang J, Geng J, Jin P, Cui L, Jiang B, Collu M. Optimal design and performance analysis of a hybrid system combining a floating wind platform and wave energy converters. *Applied Energy* 2020. <https://doi.org/10.1016/j.apenergy.2020.114998>.
30. Zhou B, Hu J, Jin P, Sun K, Li Y, Ning D. Power performance and motion of a floating wind platform and multiple heaving wave energy converters hybrid system. *Energy* 2023. <https://doi.org/10.1016/j.energy.2022.126314>.